Supplementary Information for

Electronic and Thermodynamic Properties of Native Point Defects in V_2O_5: A First-Principles Study

Lappawat Ngamwongwan,[abc] Ittipon Fongkaew,[abc] Sirichok Jungthawan,[abc] Pussana Hirunsit,[de] Sukit Limpijumnong,[af] Suwit Suthirakun*[eg]

[a] *School of Physics, Institute of Science, Suranaree University of Technology, Nakhon Ratchasima 30000, Thailand*

[b] *Center of Excellence in Advanced Functional Materials, Suranaree University of Technology, Nakhon Ratchasima 30000, Thailand*

[c] *Thailand Center of Excellence in Physics, Ministry of Higher Education, Science, Research and Innovation, Bangkok 10400, Thailand*

[d] *National Nanotechnology Center (NANOTEC), National Science and Technology Development Agency (NSTDA), 111 Thailand Science Park, Pathum Thani 12120, Thailand*

[e] *Research Network NANOTEC – SUT on Advanced Nanomaterials and Characterization, Suranaree University of Technology, Nakhon Ratchasima 30000, Thailand*

[f] *The Institute for the Promotion of Teaching Science and Technology (IPST), Bangkok 10110, Thailand*

[g] *School of Chemistry, Institute of Science, Suranaree University of Technology, Nakhon Ratchasima 30000, Thailand*

**E-mail: suthirak@sut.ac.th*

Content

Section S1. Calibration of U parameter

Due to an imperfection of the standard DFT with an approximated exchange-correlation functional, a well-known self-interaction error causes the failure in predicting some properties of materials especially in transition metal oxides. The DFT+U method could provide more accurate results by including the strong on-site Coulomb interaction between the localized electrons. However, the calculated results are quite sensitive to the strength of U, so that it must be chosen carefully in order to properly describe the electronic structure and properties of native point defects. In practice, U parameter could be chosen by calibrating the calculated results with the experimental ones, and it would be differed for such a property.

For V_2O_5, a wide range of U (2.0 - 6.6 eV) was utilized for V-3*d* orbitals depending on the difference of interest properties.[1-4] For instance, U = 2.0 and 3.1 eV was proposed by calibrating with overall reduction energy of vanadium oxides.[1,2] Similarly, U = 3.5 eV was nominated to provide a uniform description in overall structural parameters, band-gap energy, dielectric constant, and heat of enthalpy.[3] In addition, Scanlon *et al.*[4] suggested U of 4.0 eV for investigating the polaron formation of the reduced V_2O_5 via thermal reduction (oxygen vacancy) and chemical reduction (lithium intercalation). In particular, the strength of U was calibrated with the position of polaronic state to band-gap energy ratio in experiment. This ratio might be an appropriate criterion for describing the polaronic behavior properly. However, their model does not concern about van der Waals interaction resulting in 10% error of c parameter, which might lead to an inaccuracy in polaron behavior and lithium intercalation due to the narrower of interlayer spacing. This error can be reduced to only 1.8% by the introducing the optPBE-vdw functional.[5-7]

In this work, we parameterized the U parameter by Scanlon's criteria with the implementation of van der Waals interaction based on the experimental data. Wu *et al.*[8] studied the Li intercalation reaction in thin film V_2O_5. When one intercalated Li atom is fully ionized and donates one electron to a neighboring V center, resulting in the reduction of V (V^{5+} becomes V^{4+}), becoming the electron polaron and producing a gap state. The polaronic state can be observed by ultraviolet photoemission spectroscopy (UPS).[8] At the initial process i.e. low Li content, the polaronic state is found at around 1.2 eV above valence band maximum (VBM). This result leads us to the position of polaronic state to energy gap ratio around 0.5 for the experimental band gap of 2.4 eV.[9] This ratio was set for the criteria of parameterizing U in this work.

In order to calibrate U parameter, PBE+U where U ranging from 2.0 – 6.0 eV was used for optimizing the crystal structure and calculating DOS of pristine and Li-intercalated V_2O_5 ($Li_{0.056}V_2O_5$). From the calculated DOS of Li-intercalated V_2O_5, we find that the position of the mid gap state dramatically decreases as an increase in U whereas the band-gap energy from the pristine DOS steadily increases. Table S1 shows the trend of calculated results compared to previous calculations and experiment. Also, the positions of polaronic state and band gap energies as well their ratios are plotted as a function of U as shown in Fig. S1. The experimental ratio around 0.5 is matched to the calculated one at U around 3.5 eV. So, the appropriate U of 3.5 eV was selected to properly describe the polaronic states in this work. It should be noted that this number of U is also reported to be a better choice for explaining the structural parameters, band-gap energy, dielectric constant, and heat of enthalpy of V_2O_5.[3]

Table S1. The calculated structural parameters (lattice constants and bond lengths), band-gap energy, and the position of polaronic state position compared to the other works.

parameter	This work PBE+U/optPBE					Scanlon[4] PBE+U	Carrasco[5] PBE+U/ optPBE	Das[3] PBE+U/ D3	Exp.[10]
U (eV)	2.0	3.0	3.5	4.0	6.0	4.0	4.0	3.5	
a	11.667	11.666	11.665	11.669	11.675	11.496	11.690	11.628	11.510
b	3.598	3.613	3.621	3.629	3.656	3.630	3.628	3.615	3.563
c	4.447	4.446	4.447	4.435	4.454	4.804	4.423	4.359	4.369
V-O1	1.606	1.609	1.610	1.611	1.616	1.602	1.620	1.602	1.585
V-O2	1.800	1.804	1.806	1.808	1.817	1.805	1.810	1.798	1.780
V-O3	1.900	1.906	1.909	1.912	1.924	1.915	1.912	1.902	1.878
	2.049	2.045	2.043	2.041	2.036	2.018	2.046	2.034	2.021
E_g (eV)	1.98	2.11	2.18	2.25	2.58	2.26	2.26	2.18	2.4
polaronic state (eV)	1.89	1.31	1.09	0.85	0.20	0.91	-	-	1.2
ratio	0.95	0.62	0.50	0.38	0.08	0.41	-	-	0.5

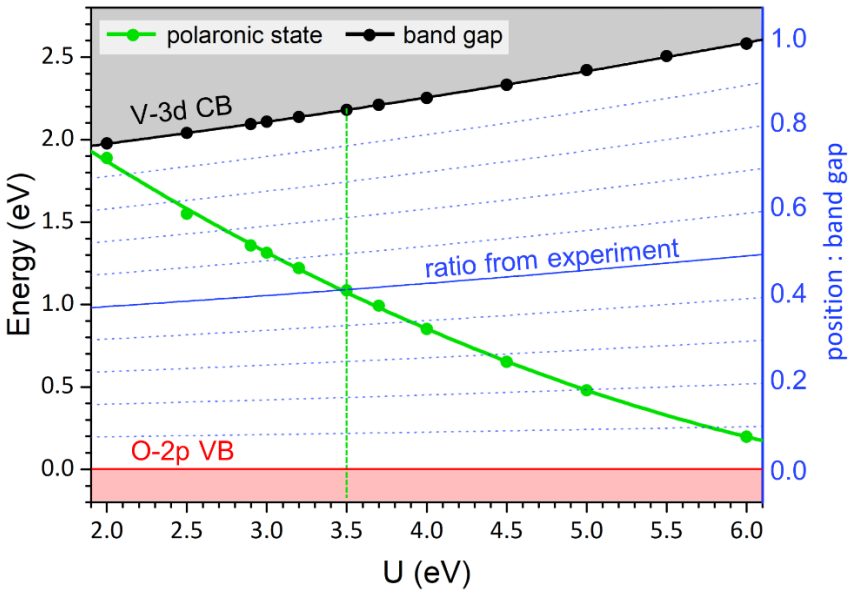

Fig. S1. Illustration of the position of polaronic state of Li-intercalated V_2O_5 and band-gap energy of pristine V_2O_5 as a function of U parameters ranging from 2.0 to 6.0 eV. The calculated position of state to band-gap ratio also plot with the experimental ratio (dotted line) in order to calibrate the appropriate U parameter.

Section S2. The effect of U_{2p}(O) on hole localization

To explore the effect of U_{2p}(O) on hole localization, we calculated the partial density of state (PDOS) of the hole-doped V_2O_5 using various U-values ranging from 0 to 8 eV. We find that the U-value greater than 3 eV generates an unoccupied gap state indicating the localization of hole polaron whereas the U-value less than 2 eV is not sufficient to localize the hole. As shown in Fig. S2a, the gap state moves further away from the VBM when increasing U-value. In particular, the hole polaron in case of U_{2p}(O) = 4 eV is shown as the example Fig. S2b-c. The PDOS indicates the hole polaronic state at 0.82 eV above VBM which is primarily the O-2*p* states, Fig S2b. The band decomposed charge density of the hole state reveals the split hole localization at three O atoms, mainly at O2 atom (Fig. S2c). Note that such split localization is previously reported in TiO_2 called a multi-site polaron.[11] Extra care needs to be taken when applying the Hubbard-U parameter in the calculations since the parameter is empirical which could lead to unphysical over-localization of hole state.

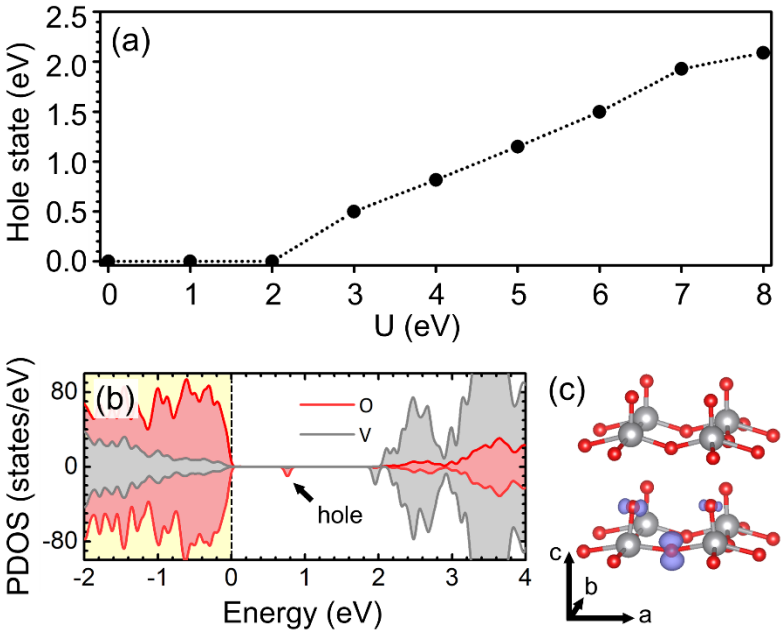

Fig. S2. (a) The hole polaronic state with respected to U-value. (b) The partial density of state of hole-doped system with U-value of 4 eV. The arrow in (b) shows the position of hole polaronic state. (c) Band decomposed charge density of the hole polaronic state as pointed out in (b). Only structures at the region near the defect site are shown for clarity.

Section S3. Band-decomposed charge density of polarons in vacancies

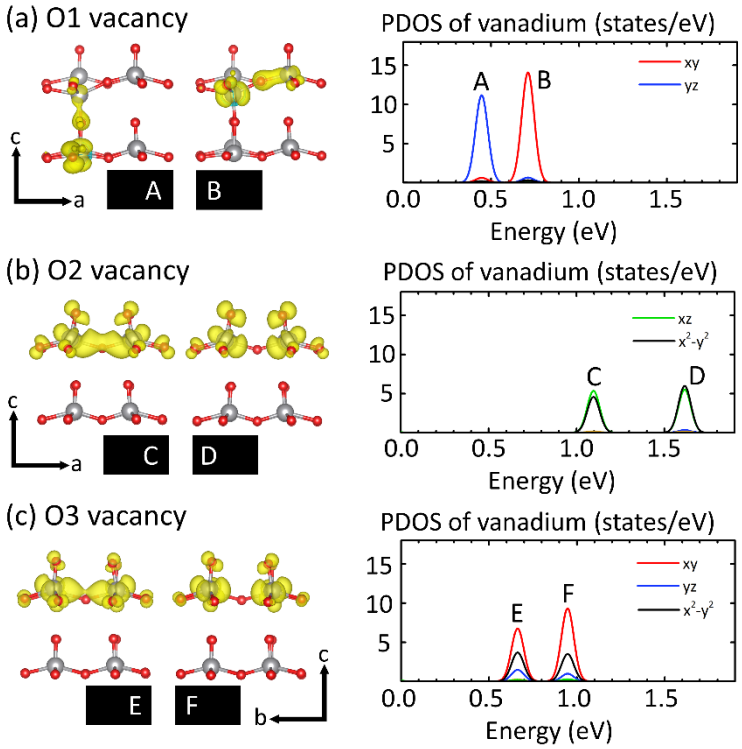

Fig. S3. [left] The band-decomposed charge densities of two polaronic states in defects O1, O2 and O3 vacancy where the isosurface level is set to be 0.002 $e^{-}/Å^{3}$. [right] The associated partial density of states (PDOS) of vanadium with orbital decomposition. Only structures at the region near the defect site are shown for clarity.

In case of O1 vacancy, there are two polaronic states lie at 0.50 and 0.76 eV above VBM. We find that the lower energy state corresponds to $3d_{yz}$ orbital of bottom V-center and the higher energy state corresponds to $3d_{xy}$ orbital of top V-center. In addition, both $3d_{xy}$ and $3d_{yz}$ normally lie in the lower splitting of crystal field. Whereas the polaronic states originated from O2 vacancy lie at 1.14 and 1.66 eV above VBM. Both polarons are formed and mainly comprises of *x*-component orbitals, i.e., the combination of $3d_{x2-y2}$ and $3d_{xz}$. This means that the two polaronic states are coupled together as the bonding and antibonding states. Likewise, the polaronic states are aligned at 0.71 and 1.00 eV above VBM for O3 vacancy. The polarons are occupied in the *y*-component orbital i.e. $3d_{xy}$ and small amount of d_{x2-y2}. The contribution of d_{x2-y2} leads to the higher energy. In addition, we also find the smaller bonding-antibonding splitting.

Section S4. Various configurations of V and O interstitial

In case of V interstitial, the position of the interstitial atom is based on the previous calculations such as Li interstitial[4] or other cations interstitial[12]. In particular, the cation (V) was inserted between the V_2O_5 layers denoted as configuration A, as shown in Fig. S4. The interstitial V atom is surrounded by 6 O atoms (4 lattice O1 atoms underneath and two lattice O2 atoms above) with the V-O bond lengths of 2.06 - 2.13 Å. As mentioned in section 3.2.C, the neutral charge V-interstitial generates 5 electron polarons where three of them localize at the three neighboring V centers and the remaining polarons are localized at the interstitial atom as shown in charge density of configuration A in Fig. S4. The polarons at neighboring site induce the interstitial atom to slightly move closer to them, leading to the non-symmetric interstitial position.

Apart from the prior insertion site, we calculated two more inequivalent configurations, B and C, as shown in Fig. S4. For configuration B, the position of V interstitial is in the same plane with 4 O1 atoms. From the top view, the off-center of interstitial is found where it moves toward O2 atoms in both layers. The total 6 V-O bond lengths are ranging from 2.02 - 2.21 Å. Unlike configurations A and B, the V interstitial links O3 atoms of both layers with V-O bond length of 2.11 and 2.15 Å. It is also surrounded by 3 O1 atoms as shown in Fig. S4 with V-O bond length around 1.91 - 1.92 Å. The calculated total energies of the configurations B and C are higher than that of the configuration A (0.78 and 0.92 eV, respectively). Such high-energy configurations might be originated from the relatively short V-O bonds and close distorted polaronic sites. Thus, among all considering configurations, configuration A is the most stable. Although, the polaronic rearrangement could give a difference in electronic energy, the configuration A with scattered polarons is a good representative for studying defect behavior of V interstitial.

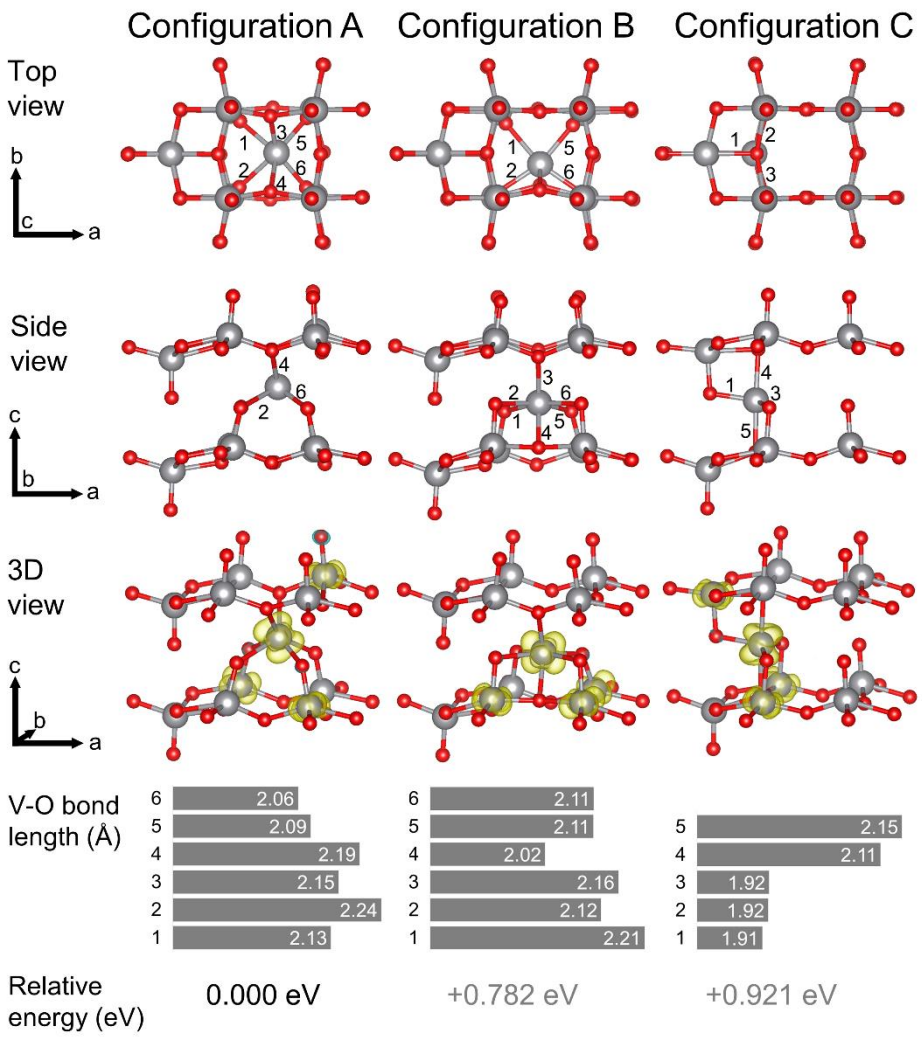

Fig. S4. The crystal structure (top, side, and 3D view) and the charge density of V interstitial in three inequivalent configurations A, B, and C. Only structures at the region near the defect site are shown for clarity. The V-O bond lengths surrounded the interstitial V atom which corresponding to the bond number labeled in the crystal structure. Also, the relative energy of each configurations compared to the lowest energy configuration.

In case of O interstitial, we inserted an O atom at the high symmetric site which surrounded by 6 O atoms (4 lattice O1 atoms of the below layer and 2 lattice O2 atoms of the above layer) as the initial configuration. After geometry relaxation, the inserted atom moves toward and bonds with one O1 atom as shown in Fig. S5, denoted as "normal O interstitial". The O-O bond is tilted from the *a*-axis to *c*-axis by 45° with the bond length of 1.33 Å and the bond length is 1.33 Å which is slightly longer than that of the O_2 molecule (1.21 Å).

We also consider the configuration where the pair of O interstitial and lattice O1 share the same O1 site which is called "O-split interstitial" as shown in Fig. S5. In this case the O-O

bond length of 1.34 Å is approximately the same to the previous case (1.33 Å), but it is parallel to the *a*-axis. We find that the energy of the O split interstitial is lower than that of the normal one by 0.36 eV. The center of the bond is at the lattice O1 site with the O and V distance of 2.00 Å. In other words, this defect can be named as a substitution of O_2 molecule at O1 site whereas the O-O bond is slightly longer than that of the O_2 molecule (1.21 Å). The normal and split interstitial configurations are reasonable because the interstitial O atom should interact with the undercoordinated O atom (O1). We find that the electronic energy of the O split interstitial becomes lower than that of the normal one around 0.36 eV. Therefore, the O split interstitial was selected as a representative for the defect.

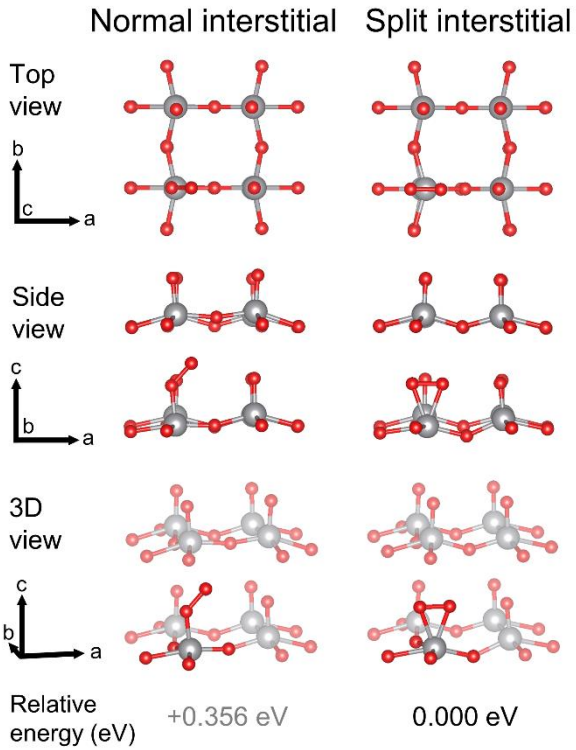

Fig. S5. The crystal structure (top, side, and 3D view) of O interstitial in two configurations which are normal interstitial and split interstitial. Only structures at the region near the defect site are shown for clarity. Also, the relative energy of each configurations compared to the lowest energy configuration.

Section S5. Density of state and band-decomposed charge density of O split-interstitial

We also try to better understand the occupied and unoccupied states of the O split-interstitial (O_i) by comparing the calculated DOS and band-decomposed charge densities with molecular orbital of the isolated O_2 molecule. In case of O_2 molecule with 8 p-electrons, 6 of them fully occupied in one σ and two π bonding states and the remaining 2 electrons separately occupied in two π antibonding states. For the O_i, the lattice O contains 2 more electrons, which is mainly taken from the ionized V, thus, the defective O_2 could have 2 extra electrons compared to O_2 molecule. Based on the charge density plots, the state lying at 0.27 and 0.43 eV are corresponding to the O-p_z and O-p_z antibonding states in spin down and spin up component, respectively, coupled with O-p_z of the in-plane O2 and O3 atoms as shown in Fig. S6B-C. While the occupied state at 0.22 and unoccupied state at 1.75 eV are related to the O-p_y and O-p_y antibonding states as shown in Fig. S6A and E. Surprisingly, the presence of occupied state at 0.62 eV is corresponded to the electron polaron from V-3d_{yz} as shown in Fig. S6D. Thus, among two extra electrons, one is formed as an electron polaron whereas only another one is filled in the O_2 defect. In other words, the defect O_2 has one more electron compared to O_2 molecule i.e. $(O_2)^-$, in which electron occupied in the antibonding state, leading to the longer O-O bond of 1.34 Å.

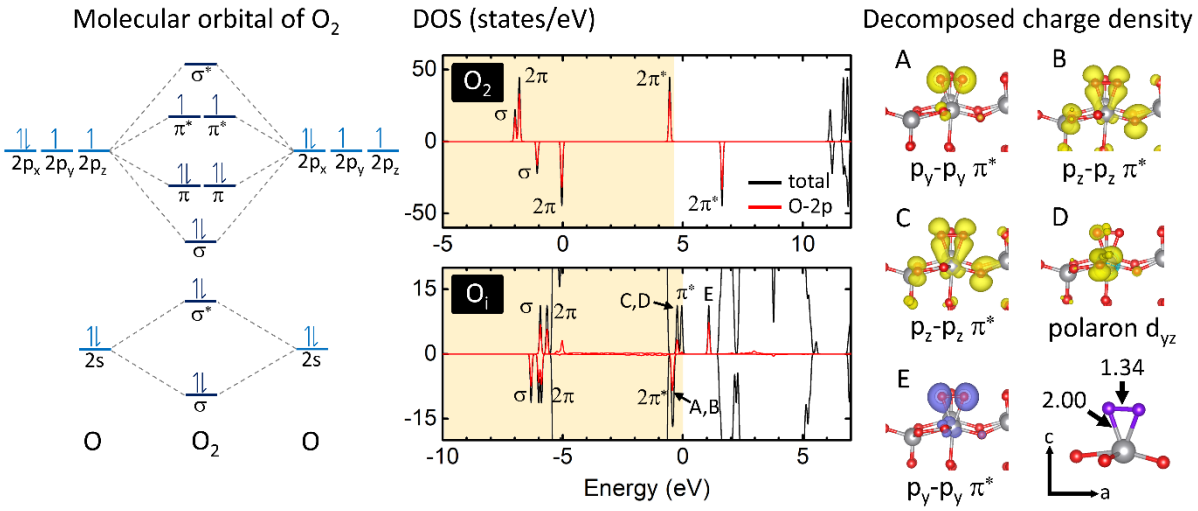

Fig. S6. [left] The schematic of molecular orbital of O_2. [middle] Density of states of O-2p orbitals of O_2 molecule and O_2 in O split-interstitial. [right] the band-decomposed charge densities of each defect state (A-E) in O split-interstitial. The isosurface level is set to be 0.002 $e^-/Å^3$ and only structures at the region near the defect site are shown for clarity.

Section S6. Chemical potentials of O at different temperature and partial pressure

The formation energy of defect is also depending on the elemental chemical potentials μ_V and μ_O. The chemical potentials are not independent due to the thermodynamic equilibrium,

$$2\mu_V(T,p) + 5\mu_O(T,p) = \mu_{V_2O_5}(T,p) \approx E_{tot}(V_2O_5),$$

where p and T are the O_2 partial pressure and temperature corresponding to the synthesis condition. $\mu_{V_2O_5}$ is the Gibbs free energy of V_2O_5. Note that the contribution of zero-point vibration and entropy of solid phase is negligible in the entire range of considered temperature, so that, $\mu_{V_2O_5}$ can be approximated to the electronic energy, $E_{tot}(V_2O_5)$. To avoid the formation of secondary phase, it is necessary to consider the upper and lower limit of $\mu_O(T,p)$. In fact, when $\mu_O(T,p)$ is too low, the V_2O_5 could be reduced to a lower-valence oxide i.e. VO_2. Therefore, the minimum of $\mu_O(T,p)$ can be defined by

$$\mu_O^{min}(T,p) = E_{tot}(V_2O_5) - 2E_{tot}(VO_2),$$

here, $E_{tot}(VO_2)$ is electronic energy of VO_2. On the contrary, $\mu_O(T,p)$ is too high or at high pressures, the oxygen gas molecules could condense on the surface instead. Thus, maximum of $\mu_O(T,p)$ can be given by

$$\mu_O^{max}(T,p) = \frac{1}{2}\mu_{O_2}(T,p) \leq \frac{1}{2}\left(E_{tot}(O_2) + E_{ZPE}(O_2)\right),$$

when $\mu_{O_2}(T,p)$ is the chemical potential of O_2 molecule depending on the condition. Note that $\mu_{O_2}(T,p)$ approaches and is no larger than the electronic energy of O_2 molecule, $E_{tot}(O_2)$.

To avoid the well-known over binding energy of O_2 molecule, we used the experimental binding energy of 5.23 eV subtracted by two times of energy of isolated oxygen atom.[2,13] Thus, the calculated $E_{tot}(O_2)$ is -4.78 eV. We note that the reduction enthalpy of V_2O_5 to VO_2 is improved by using this method (-1.02 eV and -0.40 eV for with and without correction compared to the experimental data of -1.28 eV).[1] With the calculated $E_{ZPE}(O_2)$ of 0.096 eV, we obtained μ_O = -2.34 eV for μ_O maximum. In the defect formation energy calculation, we mainly consider at the boundaries, where μ_O = -3.41 and -2.34 eV corresponds to the O-poor and O-rich condition, respectively.

It should be noted that O-rich limit at a given T and p is equaled to a half of $\mu_{O_2}(T,p)$ which can be approximated by

$$\mu_{O_2}(T,p) = E_{tot}(O_2) + E_{ZPE}(O_2) - k_B T \ln Q + k_B T \ln p,$$

when $E_{ZPE}(O_2)$ is calculated zero-point energy of O_2 and Q is the multiplication of translational, rotational, and vibrational partition function while k_B is Boltzmann's constant.

Fig. S7 shows the chemical potential range that allow the formation of V_2O_5 without formation of secondary phase. The range is limited by the O-poor and O-rich conditions. Under O-poor condition, μ_O = -3.41 eV, it is in thermodynamic equilibrium between formation of V_2O_5 and VO_2. Beyond this, the reaction shift to VO_2 formation. On the contrary, beyond O-rich condition, O_2 gas would not be reacted with V sources so that V_2O_5 cannot be occurred. Notably, μ_O at O-rich limit is depending on the synthesis condition (i.e. temperature and O_2 partial pressure). It could be approached to -2.34 eV at near absolute zero temperature. This number is associated with the total energy of O_2 molecule. Increasing in annealing temperature and decreasing in O_2 pressure can decrease μ_O at O-rich limit. In contrast, O-poor limit is independent on the growth condition. In addition, the synthesis of V_2O_5 often did under the atmospheric pressure (O_2 partial pressure = 0.21 atm) at annealing temperature ranging from 350-450 °C.[14-16] For example, the assessable range of μ_O can be variated for 0.23 eV (from -3.41 to -3.18 eV) at 450 °C. Based on the narrow range of μ_O, selecting the synthesis condition (μ_O) does not negligibly affect the energetics of point defect formation in case of normal condition.

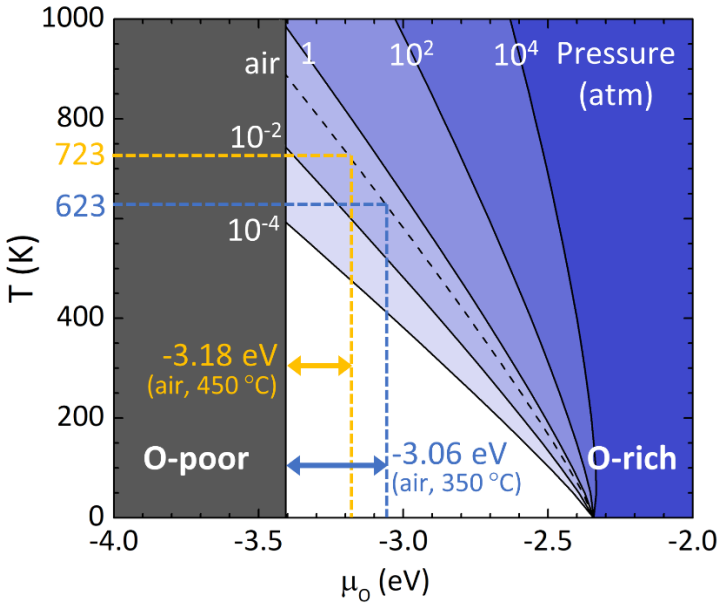

Fig. S7. The assessable range of chemical potential of O (μ_O) for V_2O_5 single phase synthesis. The range is limited by O-poor condition (gray region) at μ_O = -3.41 eV and O-rich condition (blue region) which is altered under different growth condition i.e. annealing temperature and oxygen partial pressure. The orange dashed line also shows the O-rich limit under annealing temperature ranging between 350-450 °C under air which is experimental conditions.

Section S7. Double donor O split-interstitial

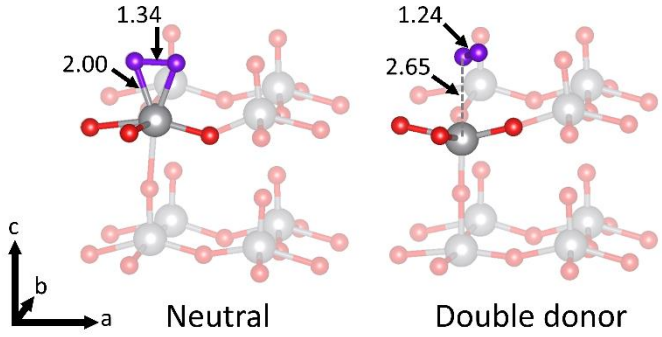

Fig. S8. The crystal structure of O split-interstitial (O_i) in [left] neutral charge state (+0) and [right] double donor (+2). Only structures at the region near the defect site are shown for clarity. The labels show associated O-O and V-O bond lengths in Angstrom. The double donor O_i decomposes into O_2 molecule adsorbed on O1 vacancy.

Section S8. Hydrogen passivation in vanadyl vacancy

Under normal synthetic conditions where water is likely present, the uncoordinated oxygen site in vanadyl vacancy (vac_{VO}) could be passivated by hydrogen atoms. Based on the local structure of vanadyl vacancy (vac_{VO}) as shown in Fig. S9a, the O2 atom closed to the vacancy site is undercoordinated. The H atom could readily bond with this O2 atom. So, we terminated that O2 atom by adding a H atom nearby denoted as H-vac_{VO}, resulting in the optimized structure as shown in Fig. S9b. The terminated H atom and O2 bond length is 0.99 Å, which pointing toward an O3 atom in the plane. The electronic structure of H-vac_{VO} exhibits two unoccupied gap state above VBM which is similar to that of the vac_{VO} as shown in Fig. S9c-d.

Next, we calculated the defect formation energy as a function of Fermi energy, similar to Fig. 3 in the manuscript. In this calculation, the condition was set to be at annealing temperature of 723 K under air (P_{O2} = 0.21 atm), e.g., μ_O = -3.18 eV. The chemical potential of hydrogen (μ_H) was carefully determined by using the equilibrium of H_2O formation as following;

$$\mu_H(T, p_{O_2}, p_{H_2O}) = \frac{1}{2}\left(\mu_{H_2O}(T, p_{H_2O}) - \mu_O(T, p_{O_2})\right)$$

The μ_{H_2O} is basically the Gibbs free energy of H_2O which included the zero-point energy and thermodynamic parameters as below;

$$\mu_{H_2O}(T, p_{H_2O}) = E_{tot}(H_2O) + E_{ZPE}(H_2O) - k_B T \ln Q + k_B T \ln p.$$

This is equivalent to the case that we did for O_2 gas in ESI section S6. The upper and lower bound of P_{H2O} was set to be 0.1 and 10^{-10} atm, resulting in the μ_H of -5.04 and -5.59 eV, respectively. blue band of formation energy. The calculated formation energy of H-vac_{VO} is plotted as a blue-shaded band in Fig. S9e which corresponds to the value between its lower and upper bound. From the graph, the defect is more stable as a double acceptor where charge state is -2 for a wide range of Fermi energy. The synthesis under higher H_2O partial pressure condition exhibits the lower formation energy of the H-terminated defect, especially at 0.1 atm. Compared to the vac_{VO}, the H-vac_{VO} is thermodynamically more favorable at Fermi energy below 2.0 eV, i.e., in case of P_{H2O} = 0.1 atm. Although the stability of the defect increases when it is terminated by H, it is significantly less stable than other defects such as vac_{O1} and η^-. Noted that the H-vac_{VO} could be formed much easier in H-rich condition such as under H_2 atmosphere. Indeed, one may avoid the formation of both acceptors H-vac_{VO} and vac_{VO} which could lower the polaron mobility.

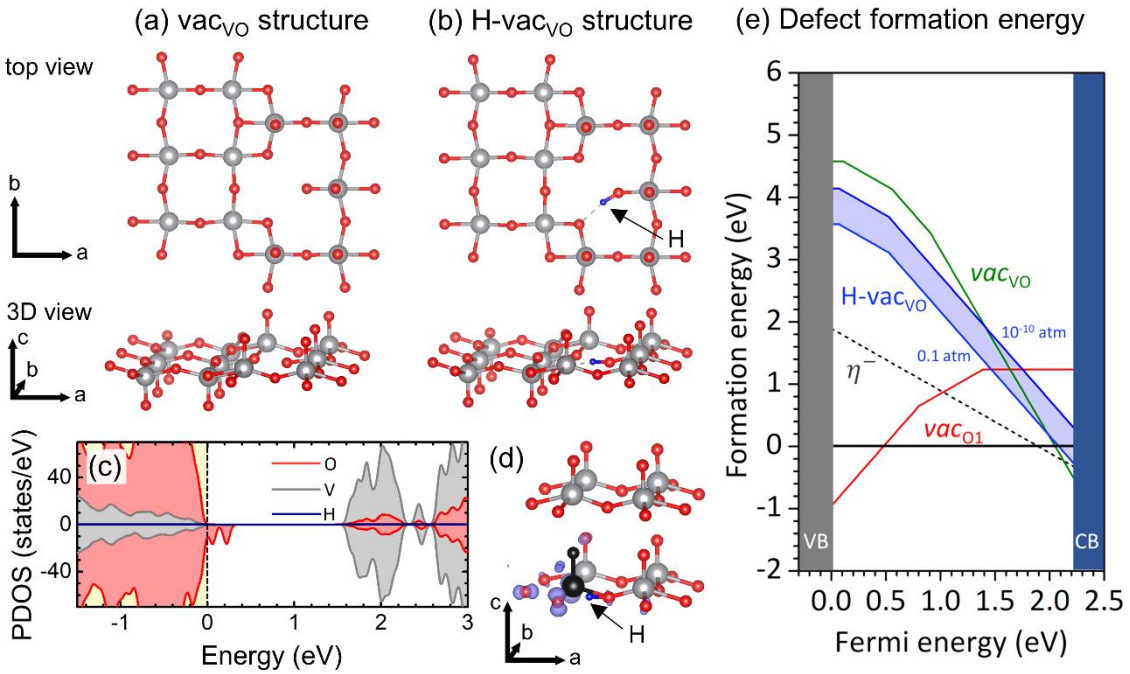

Fig. S9. The crystal structure (top and 3D view) of (a) VO vacancy denoted as vac_{VO} and (b) H-terminated VO vacancy denoted as H-vac_{VO} with a H atom terminated at the undercoordinated O2 atom. Only structures at the region near the defect site are shown for clarity. (c-d) The PDOS and unoccupied band decomposed charge density of neutral H-vac_{VO}. (e) The formation energy of H-vac_{VO} as a function of Fermi energy compared to that of vac_{VO}, vac_{O1}, and η^-. The experimental condition was set to be at annealing temperature of 723 K under normal air (P_{O2} = 0.21 atm), e.g., μ_O = -3.18 eV. The μ_H was calculated under the equilibrium of H_2O formation which corresponded to P_{H2O} = 0.1 to 10^{-10} atm, resulting in the blue band of formation energy.

Section S9. Concentrations under thermodynamic equilibrium

Previously, the formation energies of point defects as well as the lowest-energy species are depending on the position of fermi level. In order to pin the position of fermi level under thermodynamic equilibrium, we followed the procedure as proposed recently.[17] In fact, the equilibrium fermi level and defect densities at a given temperature and experimental condition can be estimated by imposing the constraint of charge neutrality when the total concentration of electrons, from both donors and thermal excitation, is equaled to the total concentration of holes, from both acceptors and thermal excitation, i.e.

$$n_e - n_h + \sum_i N_i \cdot q_i = 0.$$

Here, n_e (n_h) is the concentration of electron (hole) generated from thermal excitation which can be expressed by using the statistical equations:

$$n_e = \int_{E_g}^{\infty} f_e(E) D(E) dE \ ;$$

$$n_h = \int_{-\infty}^{0} (1 - f_e(E)) D(E) dE \ .$$

Where $f_e(E) = [1 + \exp((E_F - E)/kT)]^{-1}$ is the Fermi-Dirac distribution. E_g is energy band gap and D(E) is the density of state per unit volume. The zero of energy scale is set at VBM. In addition, the concentration of a point defect species X_i at charge stage q denoted as $N_i(X_i^q)$ can be obtained by,

$$N_i(X_i^q) = N_i^0 \exp\left(-E^f(X_i^q)/kT\right);$$

when N_i^0 is the concentration of sites in the lattice which the defect can be incorporated. From above equations, the concentration of each point defect depends on formation energy with respect to fermi level E_F. Thus, one can use a numerical method to self-consistently solve position of equilibrium fermi level that satisfy the constraint of charge neutrality. As a result, one can obtain the equilibrium fermi level and concentration of defects in thermal equilibrium at a given temperature and experimental condition. It should be noted that we neglect the effect of temperature on energy band gap and volumetric expansion of the material for simplicity. For example, the experiment proposed the indirect band gap that can be variated between 2.14 eV (300 K) and 2.07 (650 K).[18]

Section S10. Single-polaron hopping

The polaron hopping from initial site (I site) to the adjacent sites in various crystallographic directions were studied using the linear interpolation (LE) scheme. In particular, the atomic coordinates are linearly interpolated between the initial and final configuration. Then, the energy profile along the hopping path is obtained through a set of static calculations. In nonadiabatic hopping, we followed the previous work where the hopping barrier is defined at the crossing point of two parabola energy curves where polaron located at initial and final sites.[19]

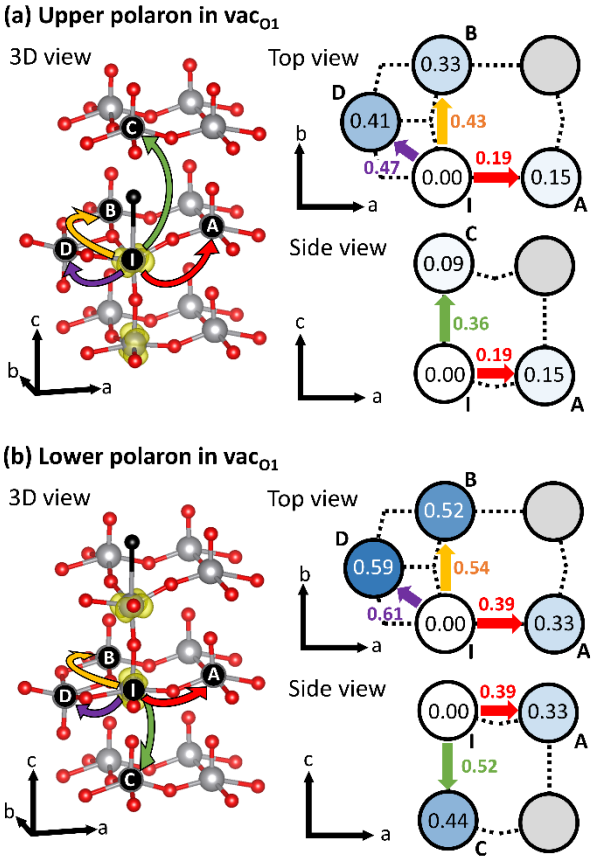

Fig. S10. Illustration of polaron hopping paths from the initial site (I) to the neighboring sites along each direction (A-D sites) and the energetic diagram of the corresponding electronic energies and the hopping barriers for (a) the upper polaron and (b) the lower polaron in vac$_{O1}$ system.

Polaron in pristine system

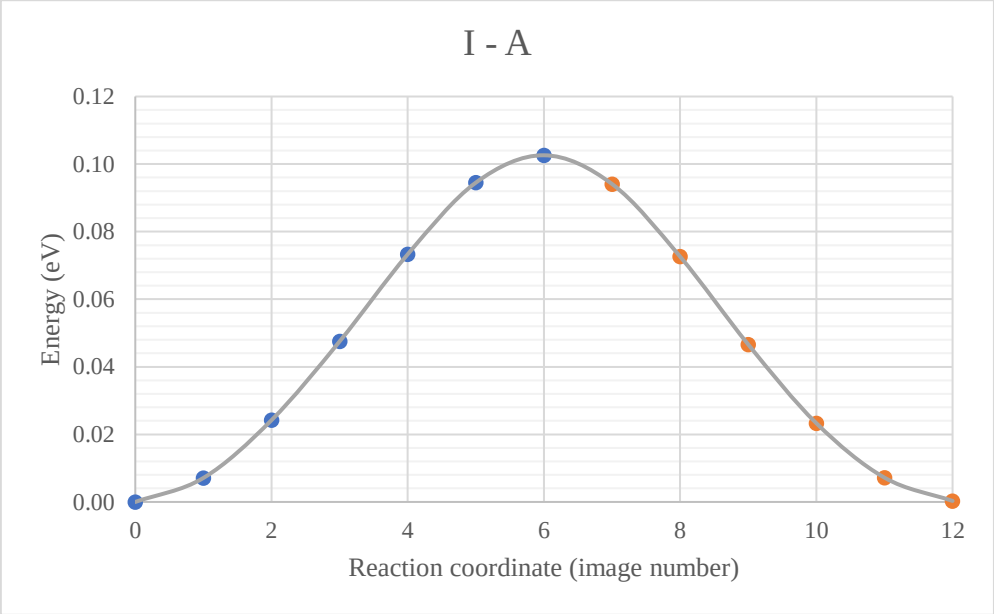

Fig. S11. Energy profile for polaron hopping from I to A site in the perfect crystal when the blue (orange) points show the major electron localization at initial (final) configuration.

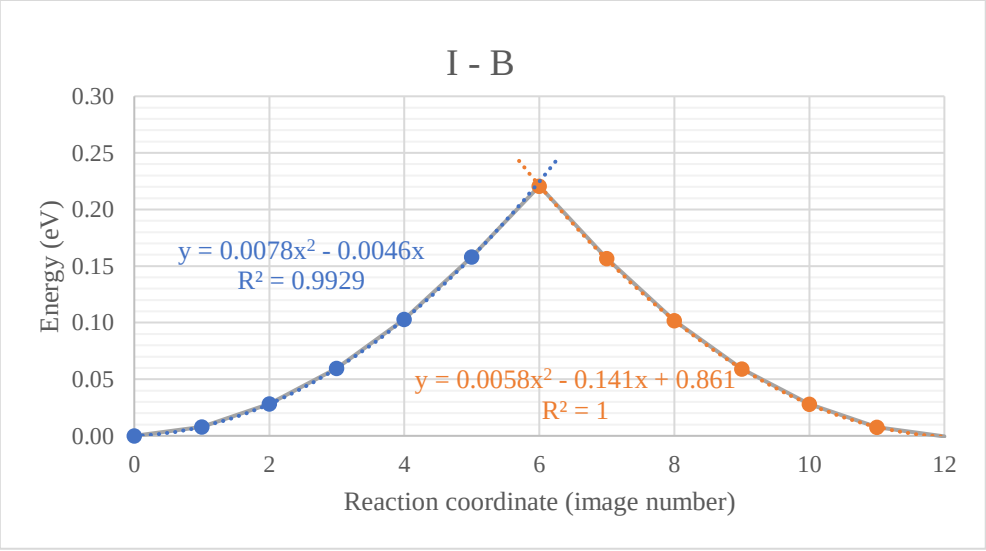

Fig. S12. Energy profile for polaron hopping from I to B site in the perfect crystal when the blue (orange) points show the major electron localization at initial (final) configuration.

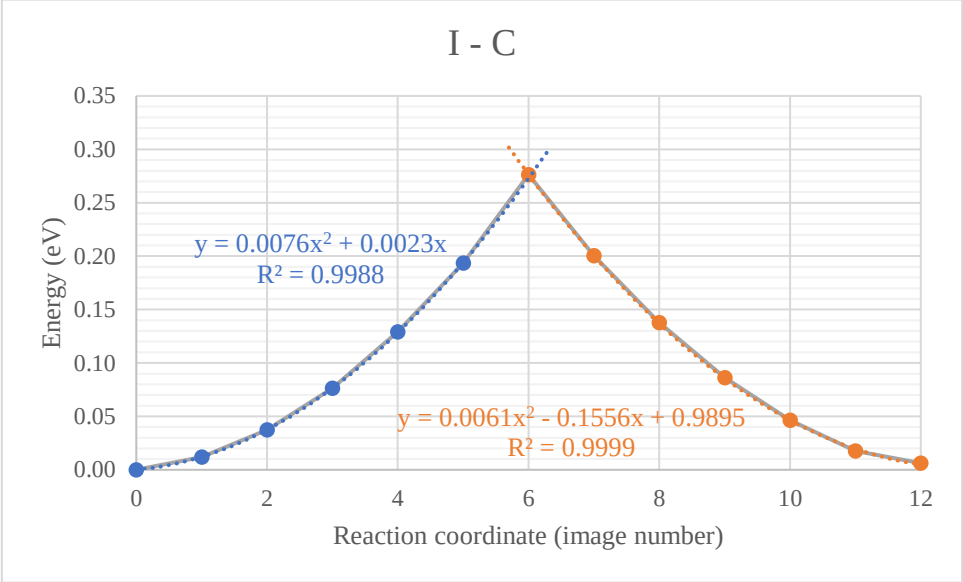

Fig. S13. Energy profile for polaron hopping from I to C site in the perfect crystal when the blue (orange) points show the major electron localization at initial (final) configuration.

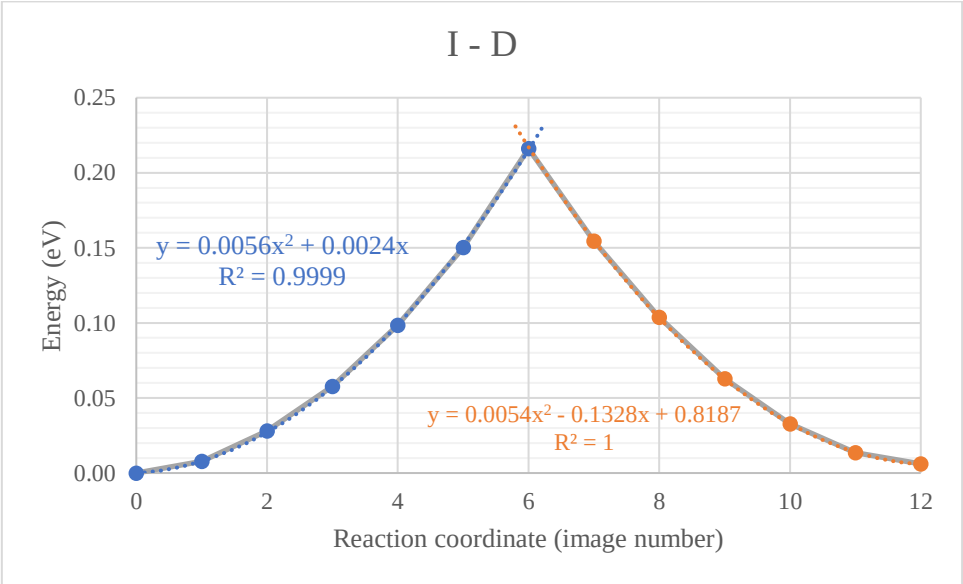

Fig. S14. Energy profile for polaron hopping from I to D site in the perfect crystal when the blue (orange) points show the major electron localization at initial (final) configuration.

The lower polaron of O1-vacancy system

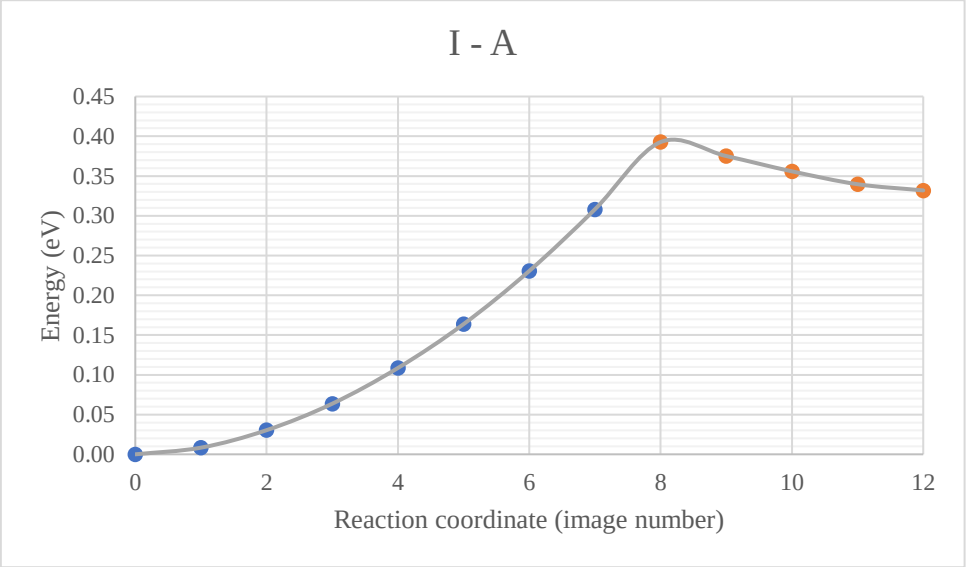

Fig. S15. Energy profile for the lower polaron of O1-vacancy hopping from I to A site when the blue (orange) points show the major electron localization at initial (final) configuration.

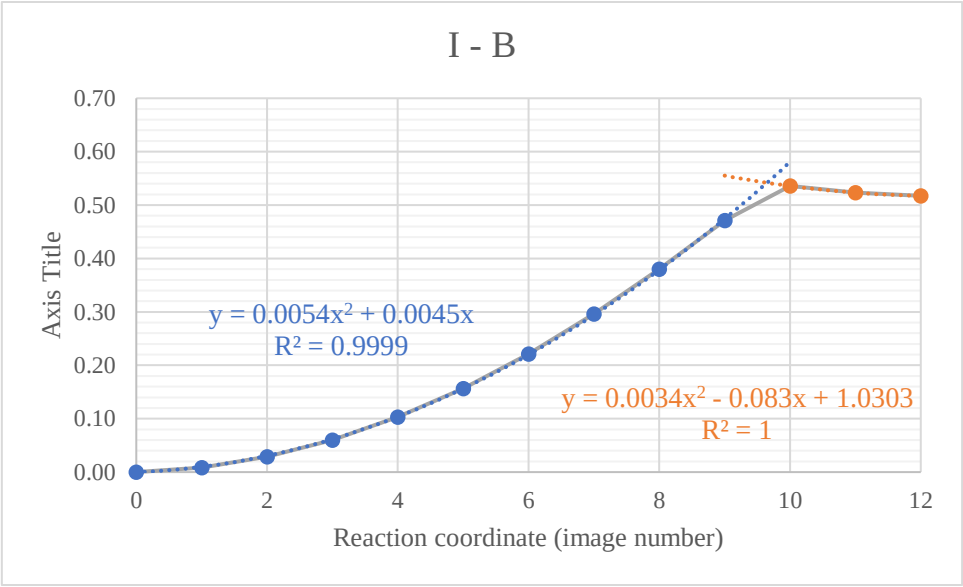

Fig. S16. Energy profile for the lower polaron of O1-vacancy hopping from I to B site when the blue (orange) points show the major electron localization at initial (final) configuration.

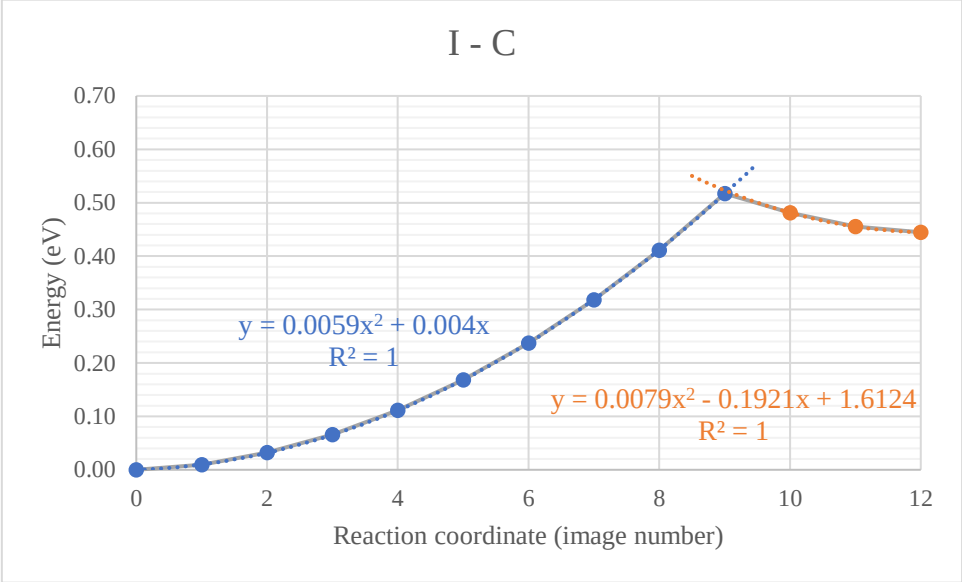

Fig. S17. Energy profile for the lower polaron of O1-vacancy hopping from I to C site when the blue (orange) points show the major electron localization at initial (final) configuration.

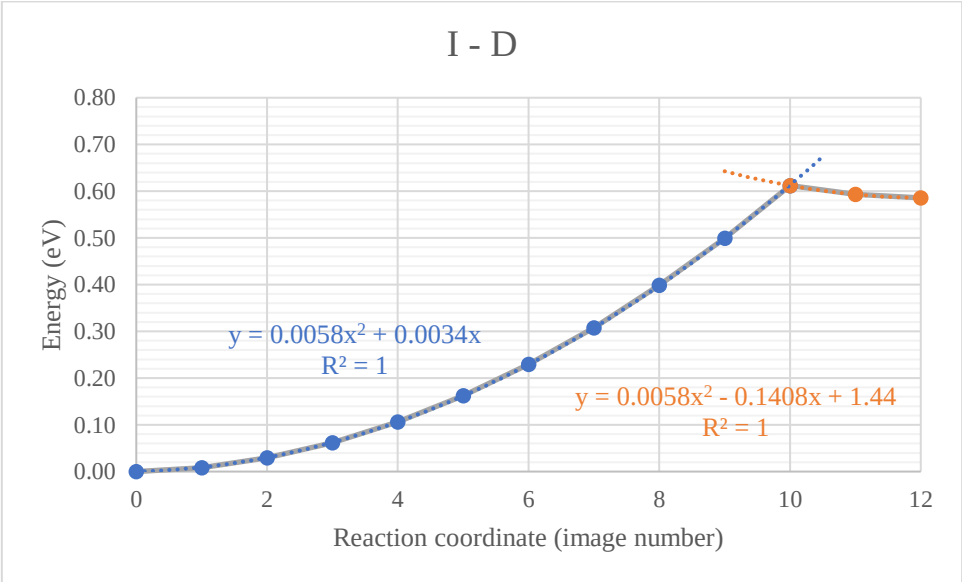

Fig. S18. Energy profile for the lower polaron of O1-vacancy hopping from I to D site when the blue (orange) points show the major electron localization at initial (final) configuration.

The upper polaron of O1-vacancy system

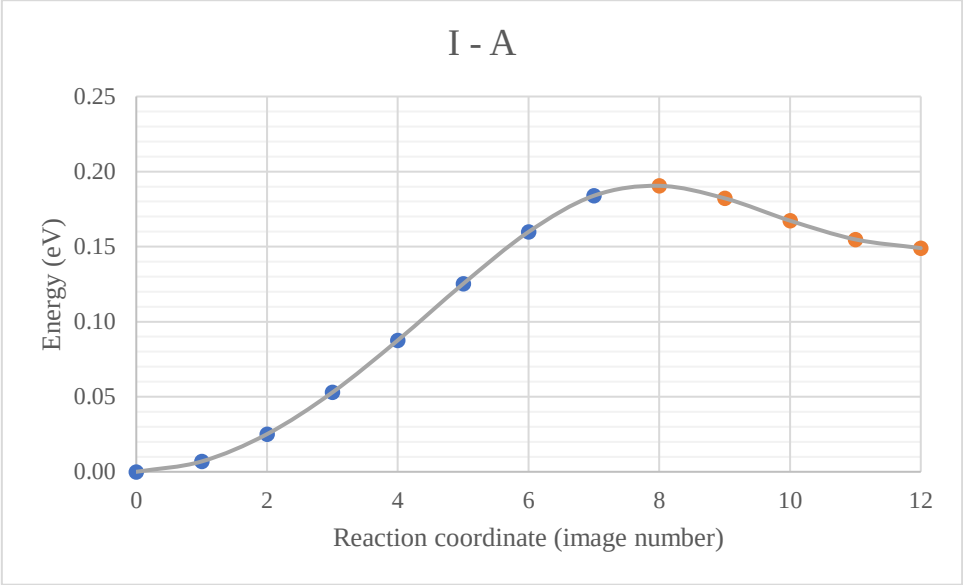

Fig. S19. Energy profile for the upper polaron of O1-vacancy hopping from I to A site when the blue (orange) points show the major electron localization at initial (final) configuration.

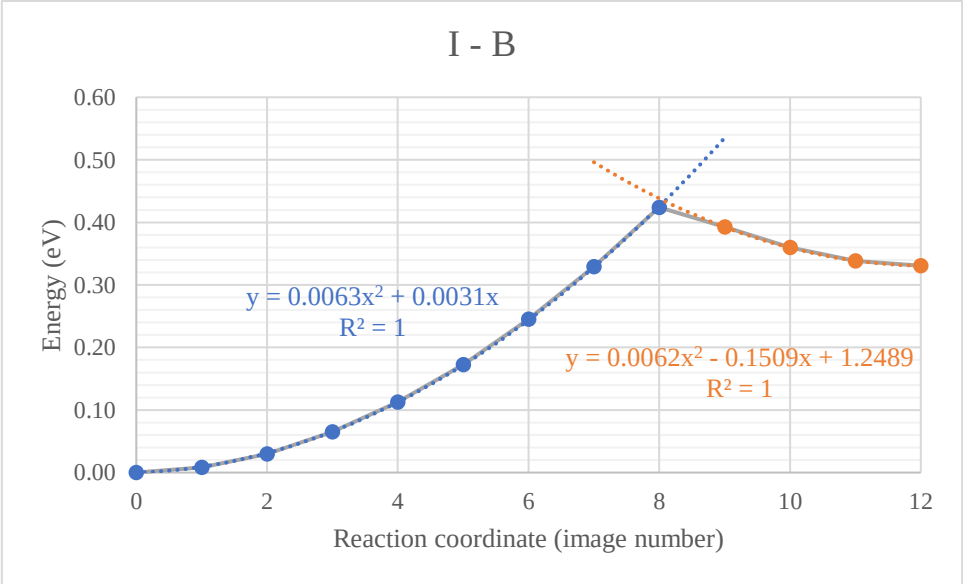

Fig. S20. Energy profile for the upper polaron of O1-vacancy hopping from I to B site when the blue (orange) points show the major electron localization at initial (final) configuration.

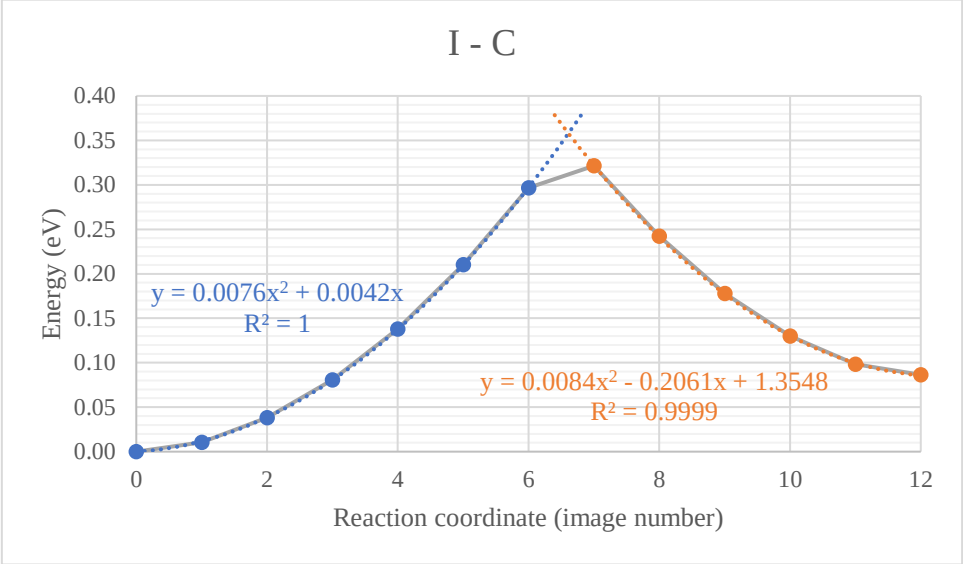

Fig. S21. Energy profile for the upper polaron of O1-vacancy hopping from I to C site when the blue (orange) points show the major electron localization at initial (final) configuration.

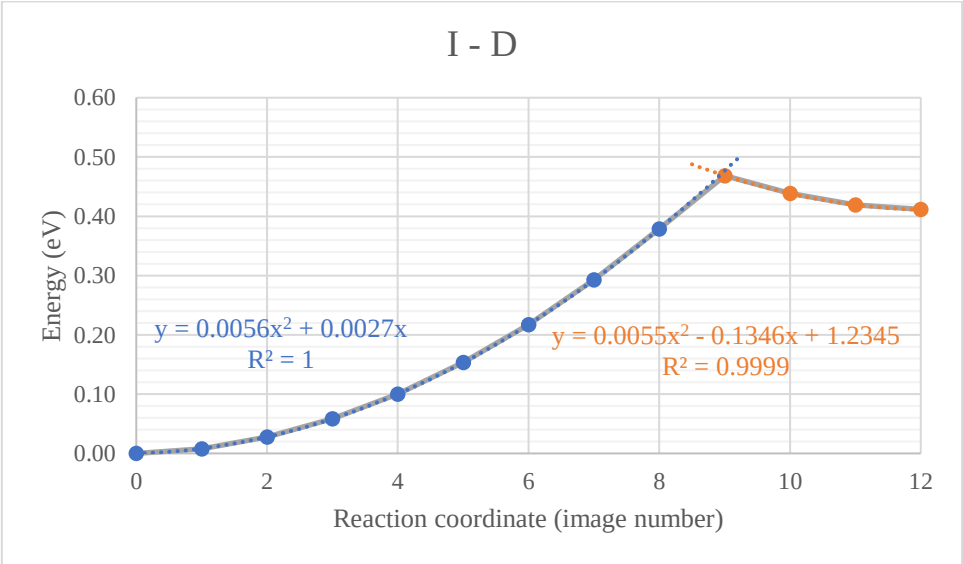

Fig. S22. Energy profile for the upper polaron of O1-vacancy hopping from I to D site when the blue (orange) points show the major electron localization at initial (final) configuration.

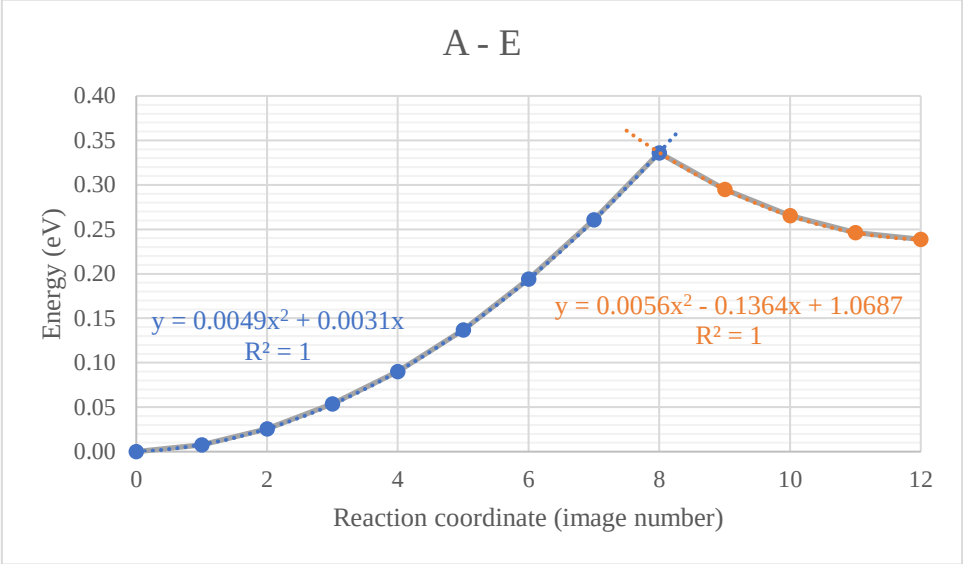

Fig. S23. Energy profile for the upper polaron of O1-vacancy hopping from A to E site when the blue (orange) points show the major electron localization at initial (final) configuration.

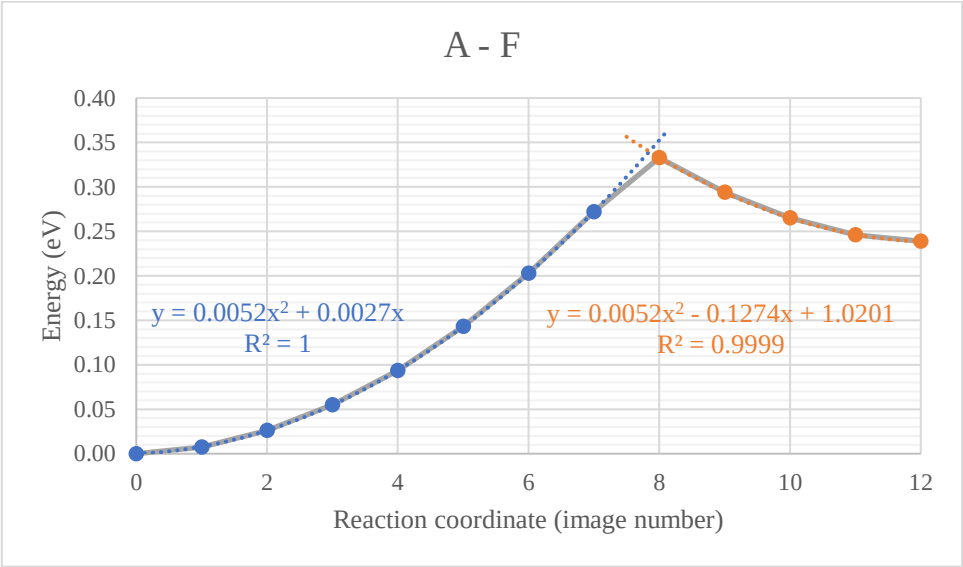

Fig. S24. Energy profile for the upper polaron of O1-vacancy hopping from A to F site when the blue (orange) points show the major electron localization at initial (final) configuration.

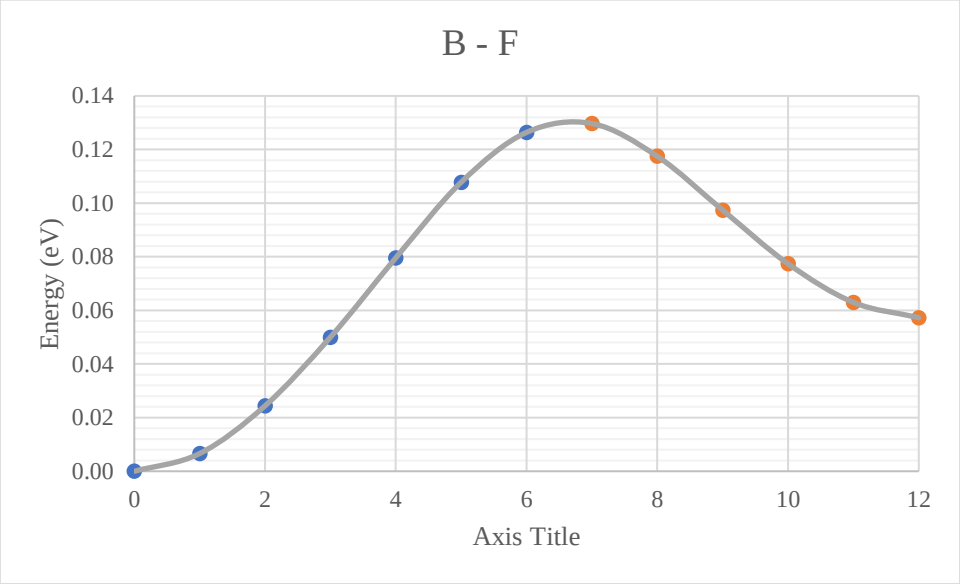

Fig. S25. Energy profile for the upper polaron of O1-vacancy hopping from B to F site when the blue (orange) points show the major electron localization at initial (final) configuration.

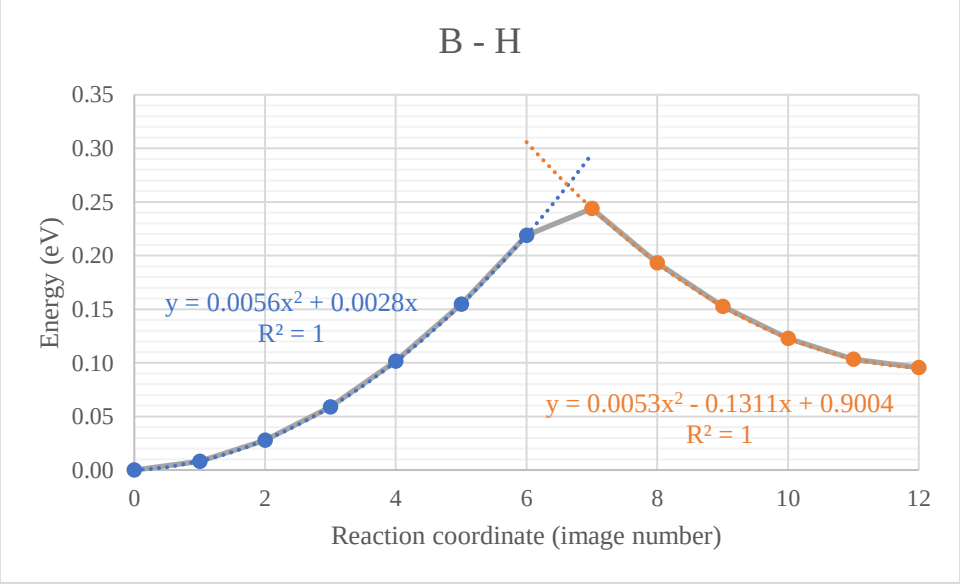

Fig. S26. Energy profile for the upper polaron of O1-vacancy hopping from B to H site when the blue (orange) points show the major electron localization at initial (final) configuration.

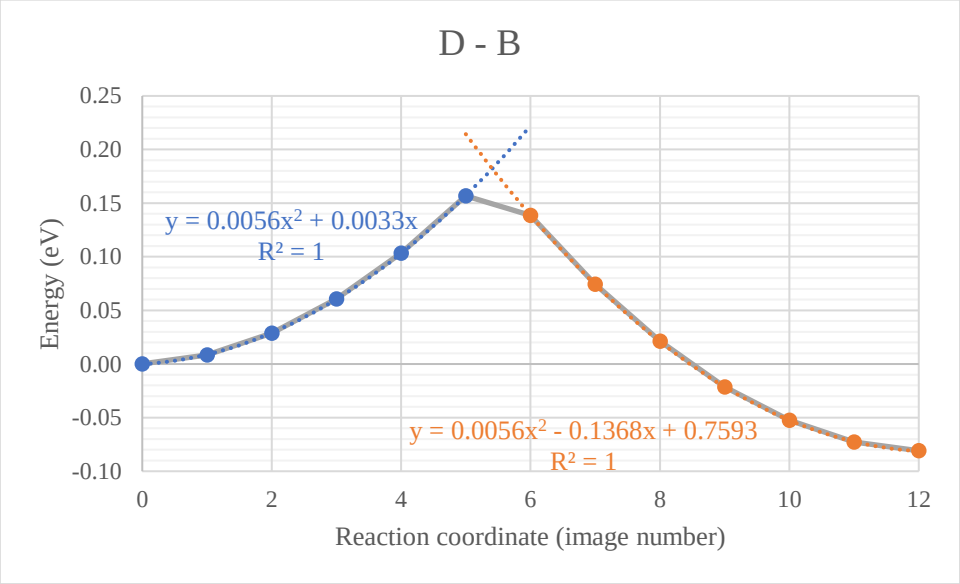

Fig. S27. Energy profile for the upper polaron of O1-vacancy hopping from D to B site when the blue (orange) points show the major electron localization at initial (final) configuration.

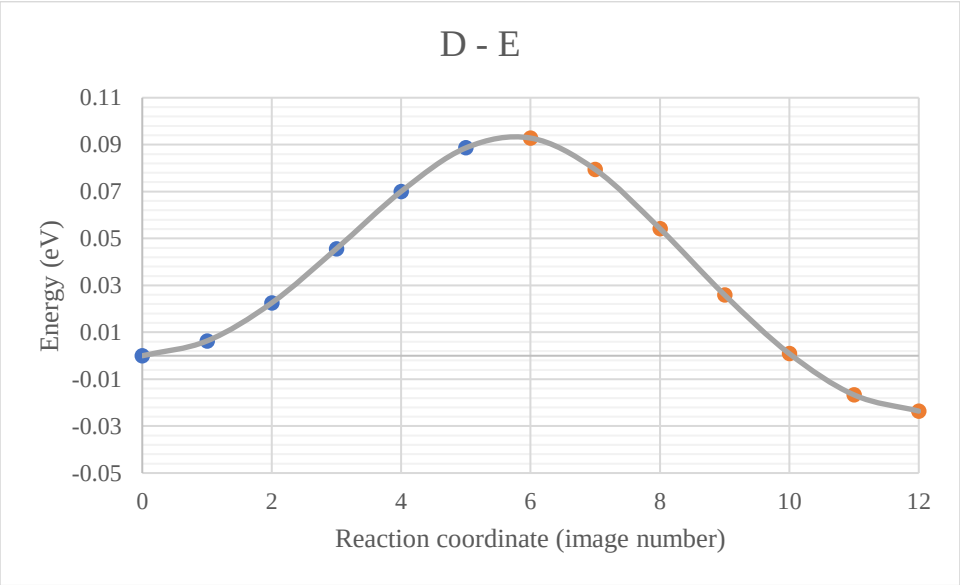

Fig. S28. Energy profile for the upper polaron of O1-vacancy hopping from D to E site when the blue (orange) points show the major electron localization at initial (final) configuration.

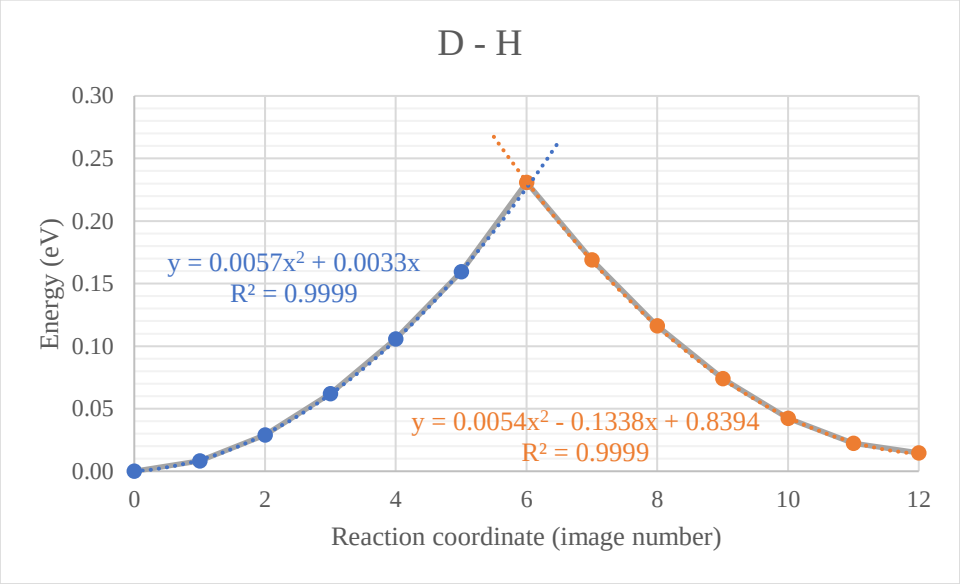

Fig. S29. Energy profile for the upper polaron of O1-vacancy hopping from D to H site when the blue (orange) points show the major electron localization at initial (final) configuration.

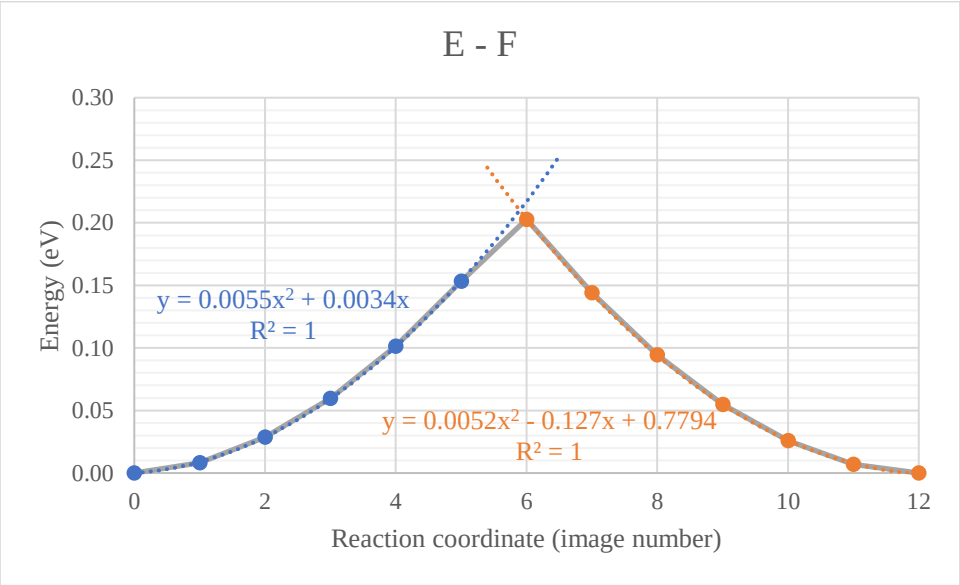

Fig. S30. Energy profile for the upper polaron of O1-vacancy hopping from E to F site when the blue (orange) points show the major electron localization at initial (final) configuration.

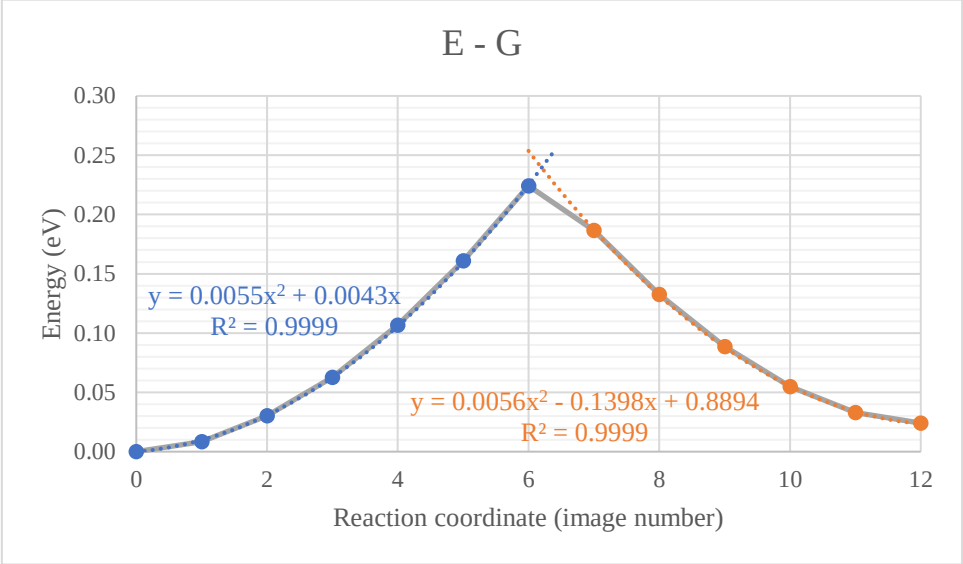

Fig. S31. Energy profile for the upper polaron of O1-vacancy hopping from E to G site when the blue (orange) points show the major electron localization at initial (final) configuration.

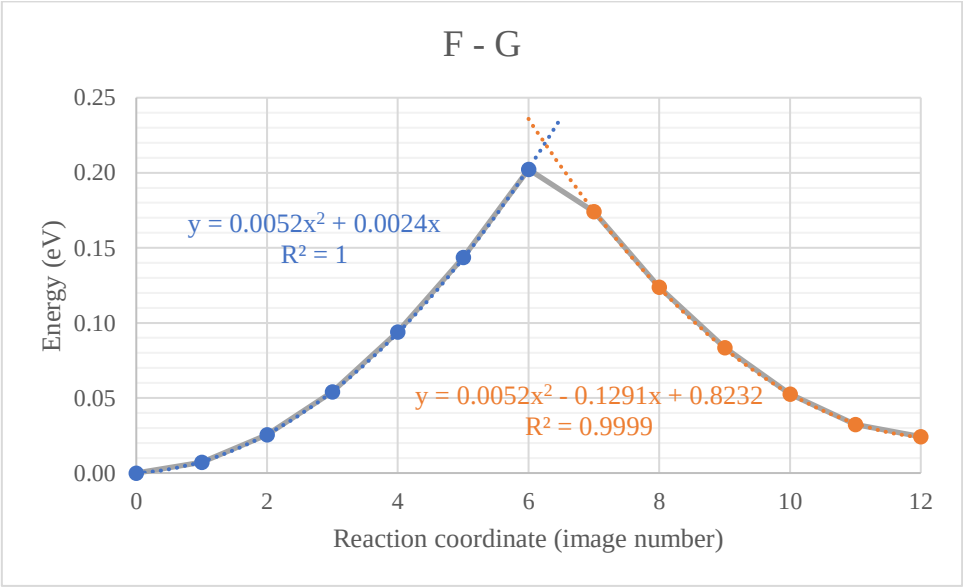

Fig. S32. Energy profile for the upper polaron of O1-vacancy hopping from F to G site when the blue (orange) points show the major electron localization at initial (final) configuration.

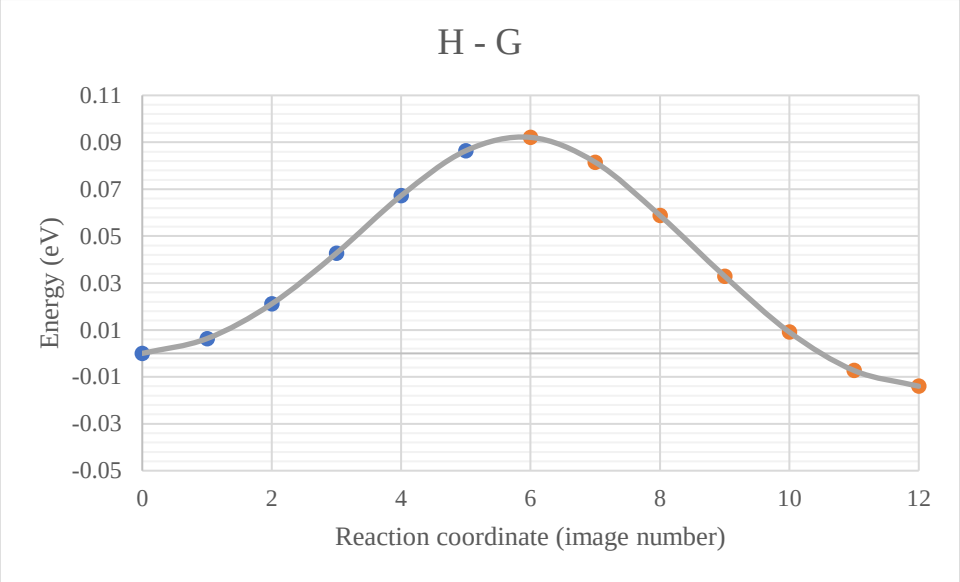

Fig. S33. Energy profile for the upper polaron of O1-vacancy hopping from H to G site when the blue (orange) points show the major electron localization at initial (final) configuration.

Table S2. The calculated reaction energies (ΔE) of polaron hopping in each considering path in case of the polaron in perfect and O1-vacancy containing system. Also, the associated energy barriers for forward direction (E_a) and reverse direction (E_r).

Polaron in perfect system

path	ΔE (eV)	E_a (eV)	E_r (eV)	direction
I - A	0.00	0.10	0.10	[100]
I - B	0.00	0.22	0.22	[010]
I - C	0.00	0.28	0.28	[001]
I - D	0.00	0.21	0.21	[110]

The lower polaron in O1-vacancy system

path	ΔE (eV)	E_a (eV)	E_r (eV)	direction
I - A	0.33	0.39	0.06	[100]
I - B	0.52	0.54	0.02	[010]
I - C	0.44	0.52	0.08	[001]
I - D	0.59	0.61	0.02	[110]

Table S2 (Cont.): The calculated reaction energies (ΔE) of polaron hopping in each considering path in case of the polaron in perfect and O1-vacancy containing system. Also, the associated energy barriers for forward direction (E_a) and reverse direction (E_r).

The upper polaron of O1-vacancy system

path	ΔE (eV)	E_a (eV)	E_r (eV)	direction
I - A	0.15	0.19	0.04	[100]
I - B	0.33	0.43	0.10	[010]
I - C	0.09	0.36	0.27	[001]
I - D	0.41	0.47	0.06	[110]
A - E	0.24	0.34	0.10	[110]
A - F	0.24	0.34	0.10	[010]
B - F	0.06	0.13	0.07	[100]
B - H	0.10	0.26	0.16	[110]
D - B	-0.08	0.18	0.26	[110]
D - E	-0.02	0.09	0.11	[100]
D - H	0.01	0.23	0.22	[010]
E - F	0.00	0.21	0.21	[110]
E - G	0.02	0.24	0.22	[010]
F - G	0.02	0.22	0.20	[110]
H - G	-0.01	0.09	0.10	[100]

Section S11. Bi-polarons coupled O1 vacancy hopping

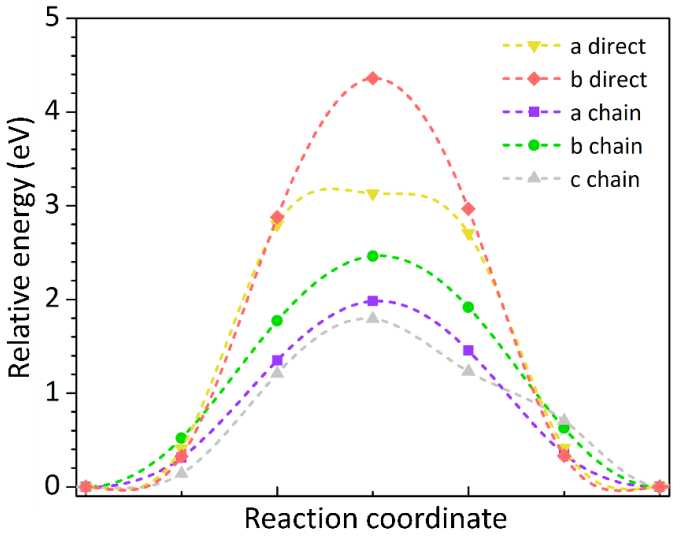

Fig. S34. Bi-polaron coupled O1 vacancy hopping along different configurations.

References

1. S. Lutfalla, V. Shapovalov and A. T. Bell, *J. Chem. Theory Comput.*, 2011, **7**, 2218-2223.
2. L. Wang, T. Maxisch and G. Ceder, *Phys. Rev. B*, 2006, **73**, 195107.
3. T. Das, S. Tosoni and G. Pacchioni, *Comput. Mater. Sci.*, 2019, **163**, 230-240.
4. D. O. Scanlon, A. Walsh, B. J. Morgan and G. W. Watson, *J. Phys. Chem. C*, 2008, **112**, 9903-9911.
5. J. Carrasco, *J. Phys. Chem. C*, 2014, **118**, 19599-19607.
6. S. Suthirakun, A. Genest and N. Rösch, *J. Phys. Chem. C*, 2018, **122**, 150-157.
7. S. Suthirakun, S. Jungthawan and S. Limpijumnong, *J. Phys. Chem. C*, 2018, **122**, 5896-5907.
8. Q. H. Wu, A. Thißen and W. Jaegermann, *Surf. Sci.*, 2005, **578**, 203-212.
9. N. V. Hieu and D. Lichtman, *J. Vac. Sci. Technol.*, 1981, **18**, 49-53.
10. H. Bachmann, F. Ahmed and W. Barnes, *Z. Kristallogr.*, 1961, **115**, 110.
11. A. R. Elmaslmane, M. B. Watkins and K. P. McKenna, *J. Chem. Theory Comput.*, 2018, **14**, 3740-3751.
12. K. McColl, I. Johnson and F. Cora, *Phys. Chem. Chem. Phys.*, 2018, **20**, 15002-15006.
13. J. Lee and S. Han, *Phys. Chem. Chem. Phys.*, 2013, **15**, 18906-18914.
14. Z. Y. Li, C. K. Zhang, C. F. Liu, H. Y. Fu, X. H. Nan, K. Wang, X. Y. Li, W. D. Ma, X. M. Lu and G. Z. Cao, *Electrochim. Acta*, 2016, **222**, 1831-1838.
15. Y. W. Li, J. H. Yao, E. Uchaker, M. Zhang, J. J. Tian, X. Y. Liu and G. Z. Cao, *J. Phys. Chem. C*, 2013, **117**, 23507-23514.
16. L. Xing, Q. Yu, Y. Bao, J. Chu, K. Han, S. Chong, C.-Y. Lao, F. Lai, P. Li, K. Xi and W. Wang, *J. Mater. Chem. A*, 2019, **7**, 25993-26001.
17. J. Buckeridge, *Comput. Phys. Commun.*, 2019, **244**, 329-342.
18. R. Basu, A. K. Prasad, S. Dhara and A. Das, *J. Phys. Chem. C*, 2016, **120**, 26539-26543.
19. V. Pasumarthi, T. Liu, M. Dupuis and C. Li, *J. Mater. Chem. A*, 2019, **7**, 3054-3065.